5-4-2020

A Physics-based Machine Learning Study of the Behavior of Interstitial Helium in Single Crystal W–Mo Binary Alloys

Adib J. Samin
Air Force Institute of Technology

Recommended Citation

Samin, A. J. (2020). A physics-based machine learning study of the behavior of interstitial helium in single crystal W–Mo binary alloys. Journal of Applied Physics, 127(17), 175904. https://doi.org/10.1063/1.5144891

Journal of Applied Physics

A physics-based machine learning study of the behavior of interstitial helium in single crystal W–Mo binary alloys

Cite as: J. Appl. Phys. **127**, 175904 (2020); https://doi.org/10.1063/1.5144891
Submitted: 12 January 2020 . Accepted: 13 April 2020 . Published Online: 04 May 2020

Adib J. Samin

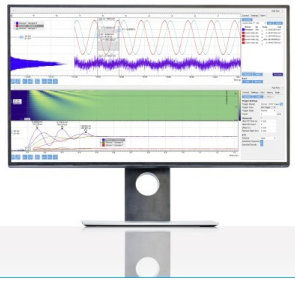

AIP Publishing

Journal of Applied Physics ARTICLE scitation.org/journal/jap

A physics-based machine learning study of the behavior of interstitial helium in single crystal W–Mo binary alloys

Cite as: J. Appl. Phys. **127**, 175904 (2020); doi: 10.1063/1.5144891
Submitted: 12 January 2020 · Accepted: 13 April 2020 ·
Published Online: 4 May 2020

Adib J. Samin[a)]

AFFILIATIONS

Department of Engineering Physics, Air Force Institute of Technology, 2950 Hobson Way, Wright-Patterson Air Force Base, Ohio 45433, USA

[a)]**Author to whom correspondence should be addressed:** adib.samin@afit.edu

ABSTRACT

In this work, the behavior of dilute interstitial helium in W–Mo binary alloys was explored through the application of a first principles-informed neural network (NN) in order to study the early stages of helium-induced damage and inform the design of next generation materials for fusion reactors. The neural network (NN) was trained using a database of 120 density functional theory (DFT) calculations on the alloy. The DFT database of computed solution energies showed a linear dependence on the composition of the first nearest neighbor metallic shell. This NN was then employed in a kinetic Monte Carlo simulation, which took into account two pathways for helium migration, the T-T pathway (T: Tetreahedral) and the T-O-T pathway (a second order saddle in both W and Mo) (O: Octahedral). It was determined that the diffusivity of interstitial helium in W–Mo alloys can vary by several orders of magnitude depending on the composition. Moreover, T-O-T pathways were found to dominate the T-T pathways for all alloy compositions for temperatures over about 450 K. Heterogeneous structures were also examined to account for radiation-induced segregation. It was observed that diffusion was fast when W segregated to the grain interior region and Mo to the grain outer region and was slow for the reverse situation. This behavior was explained by studying the energy landscape. Finally, thermodynamic simulations indicated that Mo-rich regions of the alloy were most favorable for binding the interstitial helium and may be the sites for the nucleation of helium bubbles.

INTRODUCTION

Fusion reactors offer a promising source of a sustainable, abundant form of alternative energy that does not emit greenhouse gases, reduces long-lived radioactive waste, and has limited risk of proliferation compared with fission reactors.[1] One of the important challenges with developing fusion reactors is the development of materials that can withstand harsh environments during operation.[2] Tungsten is a candidate for use in plasma-facing materials of fusion reactors due to its superior thermomechanical properties including high temperature strength, low sputtering erosion, and limited tritium retention.[3,4] Nevertheless, and despite these favorable characteristics, tungsten possesses poor toughness and a high ductile-to brittle transition temperature (DBTT) and is known to undergo significant surface morphology evolution due to its interaction with energetic helium particles, which can escape from the plasma. Helium can form bubbles, fuzz, and blisters in tungsten, which may cause its fragility and degradation, impose a limitation on its operational lifetime, and cause contamination of the plasma.[5–8] Therefore, there has recently been a growing interest in investigating tungsten alloys instead such as W–Mo,[9–12] W–Re,[13,14] W–V,[15,16] W–Ti,[17] and W–Ta alloys[18] as potential candidate plasma-facing materials. It has indeed been shown that such alloying may lead to improved characteristics compared with bulk tungsten. For example, an *ab initio* study on W–Mo binary alloys[10] and an experimental investigation of W–Mo–Cu alloys[19] revealed improved ductility compared with tungsten. El-Atwani *et al.*[20] reported that W–Ta–Cr–V alloys (38 at. % W, 36 at. % Ta, 15 at. % Cr, and 11 at. % V) displayed exceptional radiation resistance when exposed to a 1-MeV Kr^{+2} beam at 1073 K, with no signs of irradiation-induced dislocation loops after eight displacements per atom (dpa). This impressive radiation tolerance was attributed to the equal mobilities of point defects. Hasegawa *et al.*[21] observed that a small amount of rhenium (3–5) at. % in W–Re alloys was effective in suppressing void formation.

In order to assess the suitability of the material for use in fusion reactors, it is imperative to examine its interaction with helium particles and to develop and enhance our fundamental understanding of the atomistic processes that lead to bubble formation and subsequent material evolution. Such knowledge may play a vital role in informing the design of mitigation strategies and improving material performance. Despite the extensive literature reporting on helium behavior in bulk tungsten,[22–28] investigations of helium interaction with tungsten alloys have been limited. Zhang *et al.*[16] irradiated W–V binary alloys (5 wt. % V) by 60 keV He^{2+} ions. They observed reduced blistering and helium desorption compared with bulk tungsten, and this behavior was attributed to grain refinement and the alteration of trapping sites. Buzi *et al.*[17] analyzed retention properties and morphological changes after exposure to deuterium (D) and helium (He) plasma at 50 eV and surface temperatures of 500 and 1000 K and observed that nano-grained W–Ti alloys exhibited a lower concentration of blisters on their surface than pure W, including nano-grained W. Chen *et al.*[29] conducted a study on helium ion implanted W/Ni bilayer nanocomposites and concluded that dispersing nickel-nanoparticles into tungsten can protect tungsten against the deleterious effects of helium. Wu *et al.*[30] studied the effects of alloying and transmutation impurities on the stability and mobility of helium in tungsten under a fusion environment. The authors showed that 3d and 4d transition metals bind He more strongly than 5d transition metals and that He prefers to occupy sites of low charge density surrounding the impurity. They also reported a sequential relationship between diffusion energy barriers of He around the possible alloying elements as Ti > V > Os > Ta > Re. In another study, Wu *et al.*[31] also showed that the binding energies between the substitutional impurities and He increase linearly with the relative charge densities at the He occupation site, implying that He atoms easily aggregate at low charge density sites.

Density functional theory (DFT) provides a powerful tool for investigating the behavior of helium in tungsten alloys, especially considering the extreme conditions under which experiments must be performed. Furthermore, developing a complete picture of the accumulation, migration, and retention of helium in tungsten alloys begins by a detailed understanding of the mechanisms and processes governing the behavior of interstitial helium atoms in tungsten alloys. In this work, we will employ a DFT database of interstitial helium solution energies in W–Mo alloys to train a neural network (NN), which will then be utilized to explore the behavior of helium in the full range of this binary alloy.

COMPUTATIONAL METHODOLOGY

DFT calculations

Spin-polarized *ab initio* calculations were performed under the density functional theory (DFT) framework with pseudopotentials generated using Blochl's projector-augmented wave (PAW) method[32,33] as implemented in the Vienna *ab initio* Simulation Package (VASP).[34,35] The generalized gradient approximation (GGA)[36] was used for the exchange-correlation functionals as parametrized by Perdew, Burke, and Ernzerhof (PBE).[37] The first order Methfessel–Paxton method for Fermi surface smearing[38] with a small broadening width of 0.1 eV was employed in all calculations. The valence electron wave functions were expanded in a plane wave basis with cutoff energies of 500 eV. The reported DFT database was obtained by performing calculations on $4 \times 4 \times 4$ supercells (containing a total of 128 atoms), and the Brillouin zone was sampled by a Γ-centered $3 \times 3 \times 3$ Monkhorst–Pack grid.[39] The positions of the atoms as well as the volume and shape of the supercell were fully relaxed. In this work, the electronic self-consistent calculations converged to an accuracy of 10^{-7} eV, and the atomic relaxation steps (of positions and shape/size of the supercell) were allowed to continue until the total energy of the system satisfied a threshold of 10^{-4} eV between successive ionic relaxation steps. The reported solution energy for helium was obtained via the following equation:

$$E_s = E(W_{1-x}Mo_xHe) - E(W_{1-x}Mo_x) - E(He) \quad \text{for } 0 \le x \le 1, \tag{1}$$

where $E(W_{1-x}Mo_xHe)$ represents the energy of the binary alloy system containing interstitial helium, $E(W_{1-x}Mo_x)$ is the energy of the alloy supercell without the interstitial defect, and E(He) is the energy of an isolated helium atom (which was taken to be 0 eV).

The kinetics were examined by conducting a series of climbing image nudged elastic band (CI-NEB) calculations[40,41] to determine the saddle points for the interstitial helium hopping between different tetrahedral sites. The calculations were performed with the springs of elastic constants of 5 eV/Å^2 and with the optimization being performed using the quickmin method.[42] The CI-NEB calculations were performed on our $4 \times 4 \times 4$ supercells with a Γ-centered $3 \times 3 \times 3$ Monkhorst–Pack grid using the same settings as before.

Neural network model for the helium solution energy

The structure of the artificial neural network (NN) used to represent the helium solution energies is illustrated schematically in Fig. 1. The input layer contains characteristics of the local atomic environment (LAE) surrounding the interstitial defect (eight inputs were used in this work), whereas the output layer yields the associated solution energy. In between the two layers is a hidden layer containing two nodes. All nodes in each layer are connected to the nodes in the adjacent layers by real-valued weight parameters, which initially are chosen randomly. The matrix $\mathbf{W^{(1)}}$ contains the weight parameters connecting the input layer with the hidden layer (which has a size of 2×8 and 16 elements in total for our case), and the matrix $\mathbf{W^{(2)}}$ contains the weight parameters connecting the hidden layer with the output layer (which has a size of 1×2 and 2 elements in total for our case) and no bias was used in the present work. The nodes in the hidden layer and the output layer are associated with activation functions. In the illustrated NN, sigmoid activation functions were utilized for the hidden layer and a linear activation function was used in the output layer.

The input to the illustrated neural network was derived from localized clusters[43] about the interstitial atom to describe the local atomic environment (LAE) surrounding the defect. Each bcc lattice site (i) was assigned an occupation variable $\sigma_i = +1$ or -1 depending on whether it was occupied by a W (+1) or a Mo (−1) atom. Several clusters were considered in this work: the one-body figure

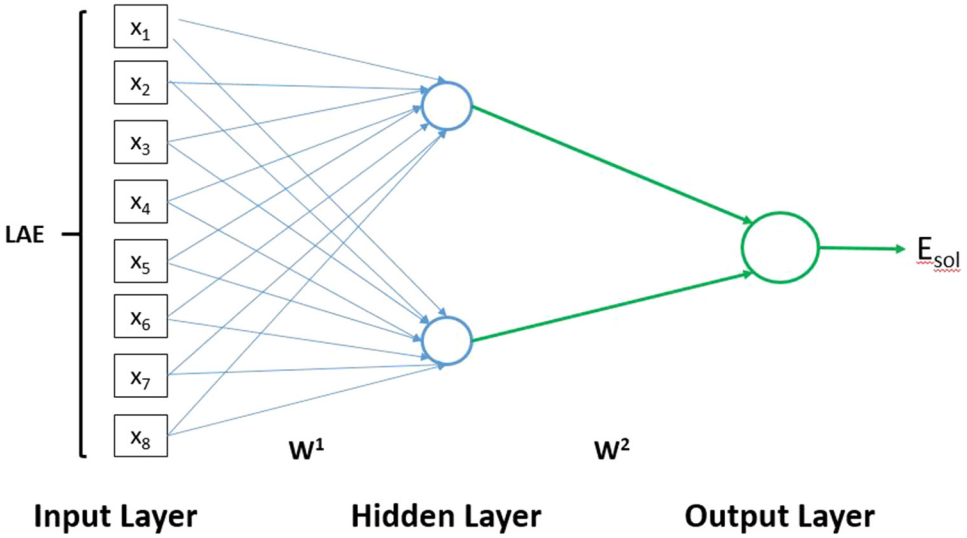

FIG. 1. An illustration of the structure of the neural network used in this work to compute the helium solution energy in W–Mo alloys after being trained with a DFT database.

(x_1) that physically corresponds to the helium occupying a T-site without interactions with any surrounding metal atoms and several two-body figures (comprising the helium occupying the T-site and one metal atom in the figure). These included the interactions of helium with metal atoms in the first, second, third, and fourth nearest neighbor shells corresponding to inputs x_2, x_3, x_4, and x_5, respectively. Three 3-body figures containing the interstitial helium at the T-site and two metal atoms were also used. These three-body clusters are illustrated in Figs. 2(a)–2(c) corresponding to inputs x_6, x_7, and x_8, respectively. In considering these local clusters (containing the tetrahedral site), equivalent structures derived from point symmetry were treated equivalently and averaged, and no translations were included because the clusters are localized about the tetrahedral site. Only T-sites were considered because T-sites bind helium more strongly than octahedral sites and, hence, it is reasonable to assume that interstitial helium atoms in dilute concentrations will occupy these sites. In constructing a representation for the solution energy, He–He interactions were ignored and hence the neural network representation is only valid in the dilute limit.

Training and data selection

For training the neural network, the backpropagation algorithm using the batch method was implemented.[44,45] In the batch method, each weight update is calculated for all the errors of the training data, and the average of the weight updates is used. The epoch identifies the number of completed training cycles for all of

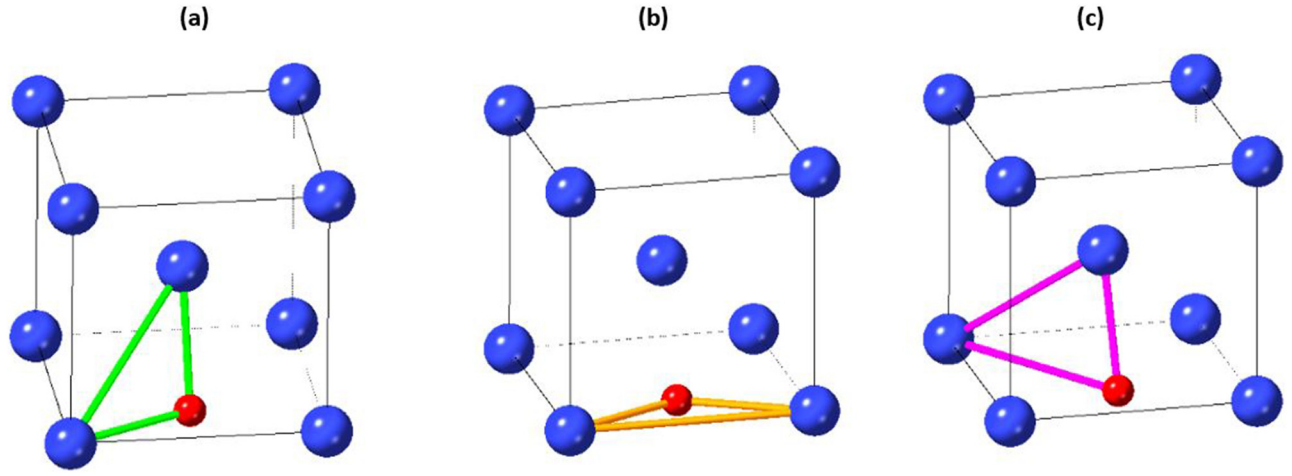

FIG. 2. An illustration of the three-body clusters used as input for describing the local atomic environment about the interstitial helium (a) was used for x_6 (b) was used for x_7 and (c) was used for x_8.

the training data. In the batch method, the number of training processes per epoch is one (since all the available training data is used to update the weights), and 200 000 epochs were used for training the neural network. At the beginning of the training process, the learning rate was 0.7 and was then increased to 0.9 after 100 000 epochs for faster convergence. The DFT data for training the neural network were selected as follows: the first 60 data points were selected by generating random structures of 25 at. %, 50 at. %, and 75 at. % tungsten and randomly placing the helium atom at a T-site. This group of data points allowed for an initial parametrization of the neural network. After this initial training was performed, the trained model was subsequently used to search for minimum energy configurations via a genetic algorithm (whose details are described in the Appendix) finding the most favorable configurations about an interstitial helium atom for a specified overall composition of the alloy. These configurations were then used as input structures for additional DFT calculations, and the output of these calculations was added to the database. This process was repeated until the neural network was able to reliably predict helium solution energies given input regarding the local atomic environment surrounding the T-site in question.

RESULTS AND DISCUSSION

The equilibrium lattice constants for tungsten and molybdenum were calculated to be 3.17 Å and 3.15 Å, respectively. These values agree with previous calculations[26,46,47] and with experimental measurements of 3.165 Å and 3.147 Å for tungsten and molybdenum, respectively.[48] Helium solution energies in bulk bcc tungsten and bulk bcc molybdenum were computed using both the PBE density functional[37] and the Perdew–Wang (PW91) density functional[49] according to Eq. (1). Both the tetrahedral sites (T-sites) and octahedral sites (O-sites) were examined. The results were recorded in Table I and compared to other calculations in the literature. All calculations performed in this work were found to be non-magnetic.

The results of Table I indicate that our calculations are consistent with the literature and that the T-sites are more stable than the O-sites for helium binding in both tungsten and molybdenum.[26,51–53] Furthermore, the relative values for the solution energy of helium in T-site compared to O-site are consistent for the two density functionals. For the remainder of this work, we chose to employ PBE exchange-correlation functionals. The minor differences between calculations utilizing different density functionals are not expected to have a significant impact on the results reported in this work.

The zero-point energy corrections to the minima and the saddle points were determined by displacing the helium atom and four metal atoms and summing up the zero-point normal vibrational frequencies $E_{ZPE} = \frac{1}{2}\sum h\nu_i$, where ν_i are the frequencies of the normal modes. Our results for the zero-point energy corrections appear to be consistent with values reported in the literature for Mo[52] (none are reported in the literature for W) as shown in parentheses in Table I.

In our calculations, two different pathways were considered for helium migration in bcc W and bcc Mo. The first pathway was the T-T pathway, and the second pathway was the T-O-T pathway, which was found to be a second order saddle (associated with two imaginary frequencies). The hopping frequencies were determined via Vineyard's method[54] where the hop frequencies were found using harmonic transition state theory in the classical limit:

$$\nu_0 = \frac{\prod_{j=1}^{3N} \nu_j}{\prod_{j=1}^{3N-1} \nu_j^{\dagger}}, \tag{2}$$

where ν_j and $\nu_j^{\dagger}$ are the real normal mode frequencies at the initial state and the transition state, respectively. The results are reported in Table II, and the pathways are shown in Fig. 3.

The results reported in Table II are consistent with values reported in the literature. Becquart and Domain[26] reported a migration energy of about 0.06 eV for interstitial helium in bcc tungsten for the T-T pathway [without considering the zero-point energy (ZPE) correction]. For the T-T and T-O-T pathways of interstitial helium in bcc molybdenum, You *et al.*[52] reported migration energies of 0.06 eV and 0.17 eV, respectively (without the zero-point energy correction). After including the ZPE correction, they reported values of 0.05 eV for the T-T pathway and 0.12 eV for the T-O-T pathway in agreement with our reported results for migration energies in Mo. Runevall and Sandberg[51] calculated a migration energy of 0.053 eV for helium traveling along the T-T pathway in bcc Mo (without

TABLE I. The solution energies for helium in tetrahedral (T-site) and octahedral (O-site) interstitial sites of bcc W and bcc Mo using different density functionals. The reported results in parentheses account for the zero-point energy corrections. The other results do not.

	Bcc W		Bcc Mo	
	T-site E_{sol} (eV)	O-site E_{sol} (eV)	T-site E_{sol} (eV)	O-site E_{sol} (eV)
This work (PBE)	6.30 (6.36)	6.51 (6.52)	5.40 (5.47)	5.56 (5.58)
Literature (PBE)	6.23,[a] 6.36[b]	6.48,[a] 6.58[b]	N/A	N/A
This work (PW91)	6.17	6.37	5.29	5.45
Literature (PW91)	6.16,[c] 6.19[d]	6.38,[c] 6.41[d]	5.33,[d] 5.28,[e] 5.39 (5.47)[f]	5.48,[d] 5.45,[e] 5.56 (5.59)[f]

[a]Lee *et al.*[46]
[b]Zhao *et al.*[50]
[c]Becquart *et al.*[26]
[d]Zu *et al.*[47]
[e]Runevall *et al.*[51]
[f]You *et al.*[52]

TABLE II. The migration energies for the T-T and T-O-T pathways interstitial helium in bcc W and bcc Mo with and without the zero-point energy (ZPE) corrections calculated via the climbing image nudged elastic band (CI-NEB) method. The hopping frequencies calculated through Vineyard's method[54] are also reported.

	BCC W		BCC Mo	
Pathways	T-T	T-O-T	T-T	T-O-T
Migration energy (eV)	0.065	0.2044	0.051	0.15
Migration energy (eV) (with ZPE correction)	0.081	0.154	0.0397	0.1
Hopping freq (Hz)	1.1×10^{12}	8.4×10^{13}	5.6×10^{12}	9.6×10^{13}

considering the ZPE correction), which again agrees with our result. Finally, it is interesting to note that for both bcc W and bcc Mo, the hopping frequency for interstitial helium to migrate via the T-O-T pathway is over an order of magnitude higher than that associated with the T-T pathway. This result is expected to have some implications for the diffusion process.

The calculated database for interstitial helium solution energies in W–Mo binary alloys (whose construction was described in the Computational Methodology section) included a total of 120 entries. The reported calculations do not include ZPE corrections and are shown in Fig. 4(a). This database only considered interstitial helium atoms placed at T-sites of the W–Mo alloys. This is a reasonable assumption in the dilute limit of He concentrations since the T-sites are more stable for binding interstitial helium.

Figure 4(a) illustrates the complex behavior of helium in the binary alloy and underlines the failure of a simple interpolation of the solution energies of helium in bulk bcc W and bcc Mo in capturing the behavior of the helium in the alloy. From Fig. 4(b), there emerges a clear pattern and the solution energy generally appears to almost vary linearly with the solution energy increasing (becoming more unfavorable) with the number of tungsten atoms in the first nearest neighbor shell surrounding the T-site where the helium is located. A weaker pattern emerges from Fig. 4(c) where it still appears that the solution energy becomes more positive with increasing the tungsten occupation fraction in the second nearest neighbor metallic shell surrounding the T-site. However, it is difficult to glean any information from Fig. 4(d), and the tungsten atoms in the third nearest neighboring shell are expected to play a smaller role in determining the solution energy compared with the metal atoms in the first and second nearest neighbor shells.

The neural network was trained with this database using the backpropagation algorithm implemented with the batch procedure as described in the Computational Methodology section. The results of this fit along with the final weight parameters are illustrated in Fig. 5.

Figure 5 shows that the trained neural network model fits the DFT data well and can reasonably produce the DFT values given information about the local atomic environment as input. Figure 5(b) depicts the weight parameters that result at the end of training the neural network. Figure 5(c) is a parity plot, which gives another illustration of the capability of the model in reproducing the data. The data points appear scattered about the $y = x$ line. Figure 5(d) shows a histogram of the errors in fitting the data points. This histogram approaches a normal distribution about 0, which indicates the absence of systematic errors. The root mean square error of the fit was calculated as 0.035 eV. Finally, it is interesting to note that our observation regarding Fig. 4(b) indicating the dependence of the solution energy on the composition of the first nearest neighbor metal shell is directly reflected in the weight parameters reported in Fig. 5(b). In particular, the first two columns of matrix $\mathbf{W}^{(1)}$ (with the first column corresponding to the input from the one-body cluster and the second column corresponding to the input from the two-body cluster consisting of the He atom and the first nearest neighbor) are the largest elements in magnitude for that weight matrix consistent with our expectations.

A good measure of the predictive power of the neural network is to examine the Leave-K-out cross validation (CV) score. To examine the fit, it was chosen to randomly leave out 15% of the DFT data points used for training the neural network (18 data points), use the rest of the data to train the network, and then test its performance on the data that were left out. This process was repeated 3000 times, and the results of this analysis are included in Fig. 6.

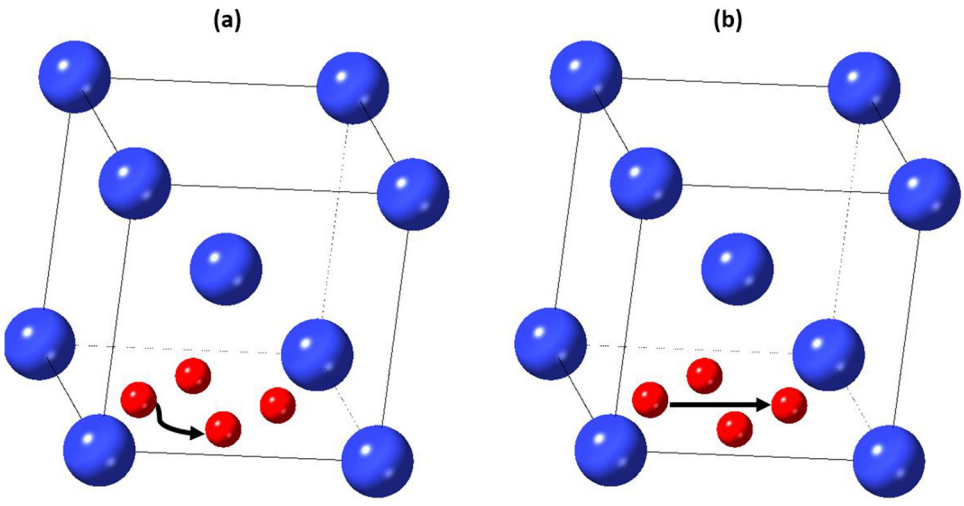

FIG. 3. An illustration of the two pathways for interstitial helium hopping in bcc W and bcc Mo: (a) the T-T pathway and (b) the T-O-T pathway.

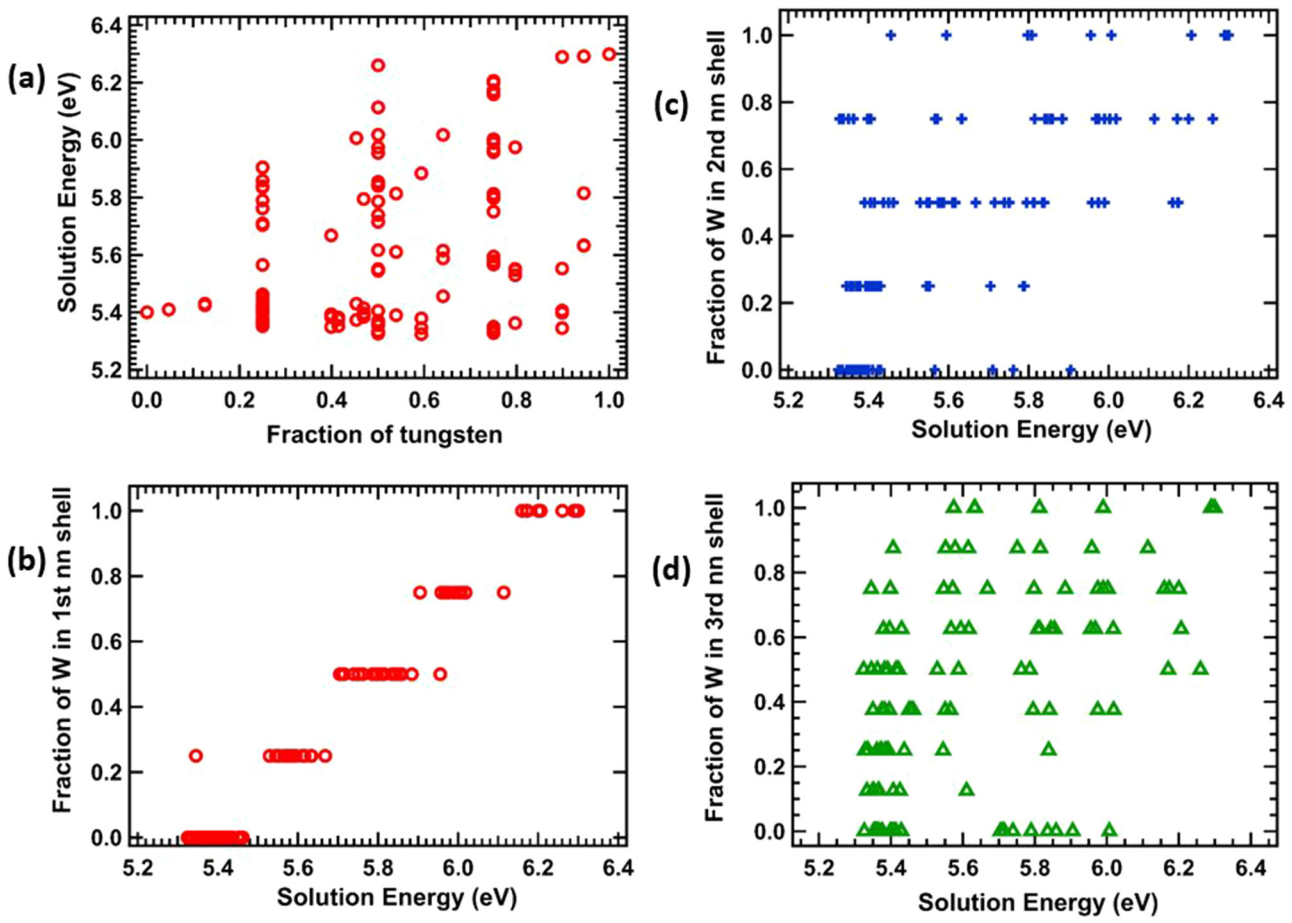

FIG. 4. (a) The DFT database (no ZPE corrections included) as a function of the global alloy composition. (b) The local atomic environment in the first nearest neighbor shell about the interstitial helium (at the T-site). (c) The local atomic environment in the second nearest neighbor shell about the interstitial helium (at the T-site). (d) The local atomic environment in the third nearest neighbor shell about the interstitial helium (at the T-site).

Figure 6(a) depicts the spread of the root mean square errors (RMSEs) of the 3000 fits performed for the 18 data points left out at the beginning of each cycle. The calculated cross validation score is 0.042 eV, and the model appears capable of predicting the left out data points well. Furthermore, another output of this analysis is 3000 sets of weight parameters. A sample of the distribution of a few of the weights is included in Fig. 6(b). It is clear from examining the figure that the fit is quite stable and that a normal distribution for each of the parameters (centered about its optimum value when all data are included) is recovered.

To analyze the diffusivity of the interstitial helium in the alloy using the neural network representation of the solution energy, a model is needed to represent the saddle point energies. The kinetically resolved activation barrier (kRA) model was used for this purpose.[43,55,56] The details of this model for calculating the saddle point energy for a hop from T-site (i) to T-site (j) are included in Eq. (3),

$$E_{barrier}(i \rightarrow j) = \begin{cases} \dfrac{E_{sol,j} - E_{sol,i}}{2} + E_o, & |E_{sol,j} - E_{sol,i}| \leq \dfrac{|E_{sol,j} - E_{sol,i}|}{2} + E_o, \\ E_{sol,j} - E_{sol,i} + 0.01\ \text{eV}, & E_{sol,j} \geq E_{sol,i} \text{ and } |E_{sol,j} - E_{sol,i}| \leq \dfrac{|E_{sol,j} - E_{sol,i}|}{2} + E_o, \\ 0.01\ \text{eV}, & E_{sol,i} \geq E_{sol,j} \text{ and } |E_{sol,j} - E_{sol,i}| \leq \dfrac{|E_{sol,j} - E_{sol,i}|}{2} + E_o. \end{cases} \quad (3)$$

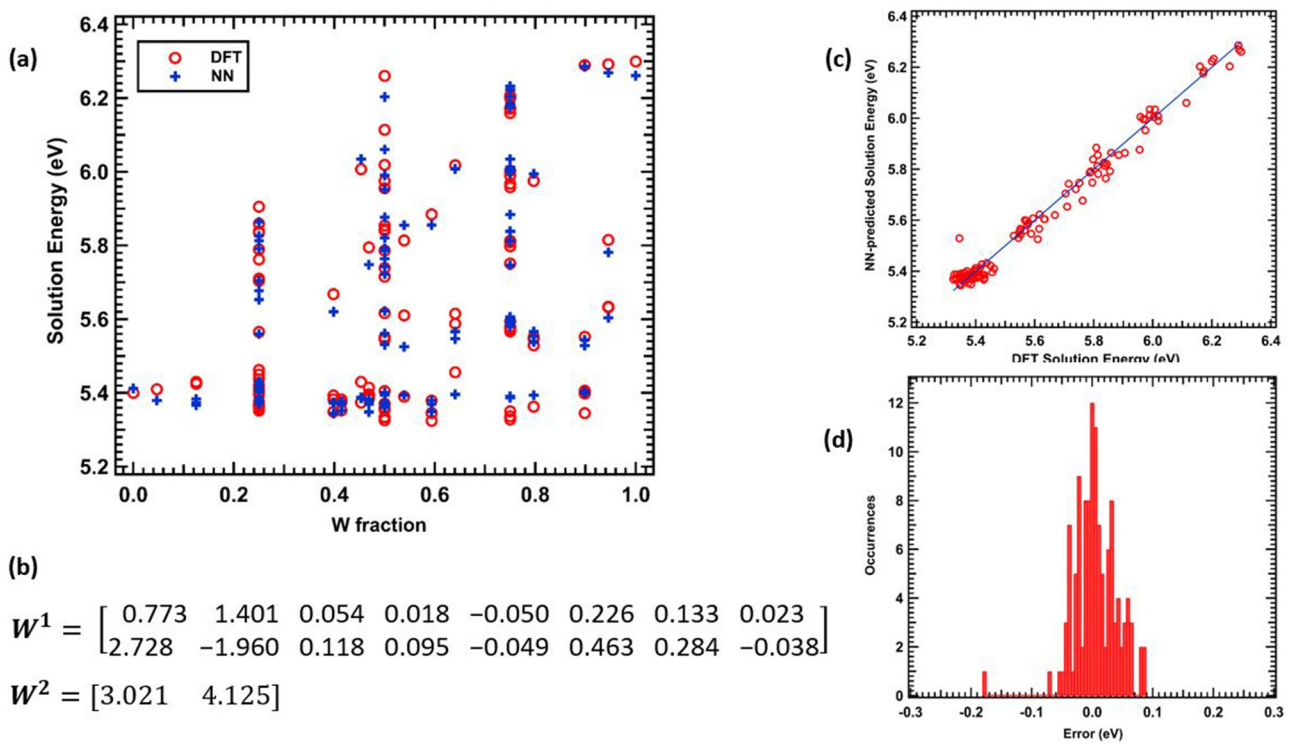

FIG. 5. The performance of the neural network trained to predict the DFT solution energy data. (a) The variation of the uncorrected (no ZPE) binding energy as a function of the global alloy composition. Both the calculated DFT results (red circles) and the neural network (NN) results (blue + signs) are shown. (b) The weight parameters that result from training the NN with the DFT database. (c) A parity plot showing the agreement between the DFT recorded data and the neural network (NN) model. The data points are clustered about the y = x line. (d) The distribution of errors at the end of training the NN.

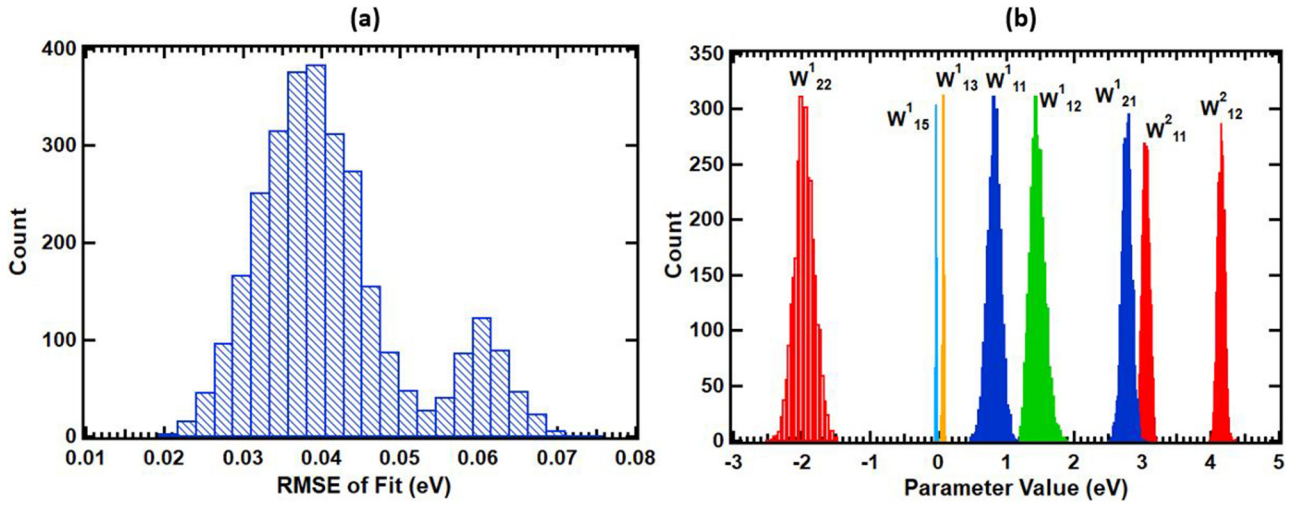

FIG. 6. Examining the prediction power of the neural network (NN) model. (a) The distribution of RMSEs after randomly leaving out 15% of the data and attempting to predict it and repeating this process for 3000 times. (b) The stability of the fit is indicated by examining the histogram of each of the 18 parameters used in this work. A sample of the distributions of these parameters as a result of the left out 15% of data cross validation analysis.

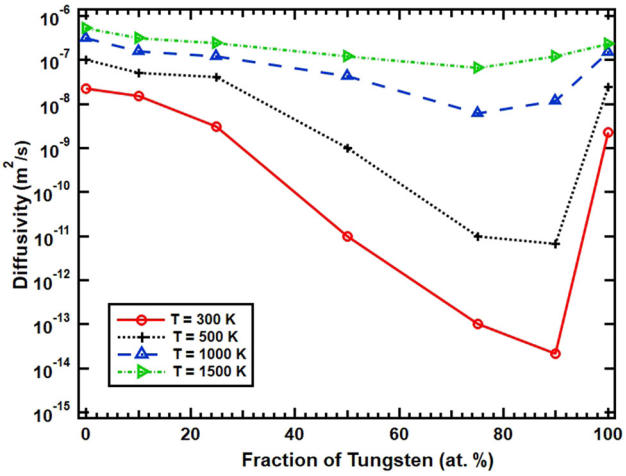

FIG. 7. The diffusivity of helium in W–Mo binary alloys as a function of temperature and composition.

E_o was obtained via interpolating between the values of the ZPE-corrected barriers for a hop in bcc W and bcc Mo (as reported in Table II) based on examining the first nearest neighbor shells for the initial and final states of the hop in the alloy. In addition, the solution energies utilized in the model (E_{sol}) were obtained from the neural network and included an additional contribution, which accounted for the ZPE corrections by interpolating between the ZPE values for He in the T-sites of bcc W and bcc Mo based on the composition of the first nearest neighbor metallic shell. In the present implementation of the kRA method, both the T-T and T-O-T pathways were accounted for and a blocking model was utilized in the kinetic Monte Carlo (kMC) simulation. In the blocking model, only one helium atom was allowed to occupy a single T-site at a time. For each concentration/temperature combination, we constructed three different random representations of the alloy and then performed kMC simulations and averaged the results. The rates used for the allowed hops in the kMC simulation are given by Eq. (4),

$$\nu = \nu_0 \exp\left(-\frac{E_{barrier}}{k_B T}\right), \tag{4}$$

with ν_0 being the frequency of the hop under consideration (T-T or T-O-T), which was also calculated by interpolating between the values in Table II based on the overall composition of the alloy and was held constant throughout the simulation. The value of $E_{barrier}$ used in Eq. (4) is derived from the kRA model [Eq. (3)].

All simulations were performed using $20 \times 20 \times 20$ supercells of the alloy with 40 He atoms diffusing (0.25 at. %) by averaging the mean square displacements of the 40 atoms collected over 1×10^8 time steps. Periodic boundary conditions (PBCs) were used in all directions for all simulations. The results of this analysis were recorded as a function of both the homogeneous alloy composition and temperature and were included in Fig. 7.

An inspection of Fig. 7 reveals the complex behavior of helium in the alloy and that a simple interpolation between the two end points is not accurate. It is clear that interstitial helium diffusivity in the homogeneous alloy can vary by several orders of magnitude depending on composition. For example, at temperature 300 K, the diffusivity can slow down by up to six orders of magnitude depending on the alloy composition. This can have significant implications for analyzing the kinetics of helium migration through the alloy and the formation of helium bubbles in the material. The results in Fig. 7 seem to indicate that the lowest diffusivity is reached when the alloy composition is in the range 75–90 at. % tungsten. Arrhenius fits of the diffusivity data reported in Fig. 7 were performed, and the results are included in Table III.

Several comments can be made with regard to the results of Arrhenius fits reported in Table III. The highest migration energy as a result of the Arrehnius fits is found to occur at around 90 at. % W. Therefore, by preparing W–Mo homogeneous alloys with 90 at. % W composition, it is possible to significantly slow down the helium migration and perhaps mitigate the damaging effects of helium interaction. Moreover, it is interesting to note that the diffusion of helium in bulk bcc tungsten and bcc molybdenum appears to be dominated by the T-O-T pathways since the activation energy obtained by Arrehnius fitting is close to the T-O-T barrier in both cases. This may be due to the relatively large attempt frequencies calculated for these hops, which are over an order of magnitude bigger than the attempt frequencies for the T-T hops. To better characterize this phenomenon, a series of kinetic Monte Carlo simulations were performed. In these simulations, the trajectory of one interstitial helium particle was tracked in a $10 \times 10 \times 10$ supercell of bcc W, bcc Mo, and several random configurations of each of the following compositions: $W_{0.75}Mo_{0.25}$, $W_{0.5}Mo_{0.5}$, and $W_{0.25}Mo_{0.75}$. Periodic boundary conditions were utilized in all simulations. Every step of the process involved six possibilities for hopping; four different options for hopping along the T-T pathway and two options for hopping along the T-O-T pathway. Each simulation tracked the helium trajectory every step of the simulation, and the simulation was performed for 10^4 steps. This process was repeated six times and the results were averaged. The goal of this simulation was to track the number of steps the particle traveled along the T-O-T relative to the total number of

TABLE III. The results of Arrhenius fits of the diffusivity data at four temperatures (T = 300, 500, 1000, and 1500 K).

At. % W	0	10	25	50	75	90	100
E_m (eV)	0.099	0.095	0.136	0.31	0.43	0.5	0.14
D_0 (m^2/s)	1.06×10^{-6}	5.4×10^{-7}	6.9×10^{-6}	1.3×10^{-6}	9.5×10^{-7}	3.5×10^{-7}	7×10^{-7}

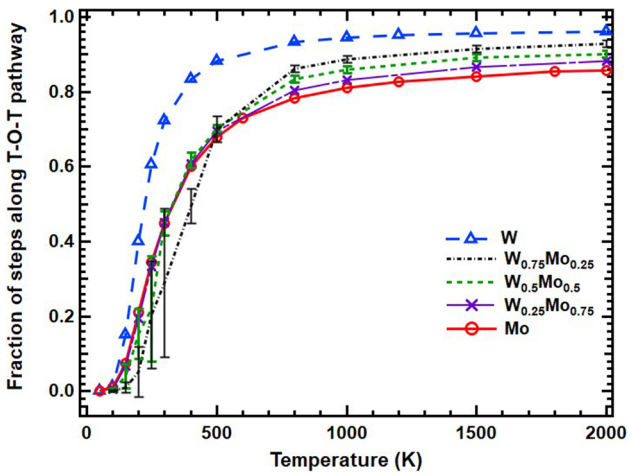

FIG. 8. The fraction of the total number of steps of the kinetic Monte Carlo (kMC) simulation traveled along the T-O-T pathway shown for interstitial helium traveling in W–Mo alloys as a function of temperature and alloy composition. Error bars correspond to standard deviations from running multiple simulations with different metallic configurations for each composition of the alloy.

kMC steps. This was recorded as a function of the simulation temperature. The results are included in Fig. 8.

The results of Fig. 8 suggest a temperature-dependent switch in the mode of migration such that the diffusion in the low temperature regime is dominated by the T-T pathway where the migration barrier is low (0.081 eV in bcc W and 0.04 eV in bcc Mo) compared with the T-O-T pathway (0.154 eV in bcc W and 0.1 eV in bcc Mo). However, once the temperature exceeds about 430 K, then the additional thermal energy allows the diffusing helium to overcome the T-O-T barrier more easily and the interstitial atoms begin to sample this pathway more frequently. From Fig. 8, it is clear that the switch from the T-T to the T-O-T migration pathway occurs at a lower temperature for helium in tungsten compared with molybdenum and molybdenum alloys. At 250 K, the fraction of T-O-T steps taken in bcc W already exceeds half of all kMC steps. This switch in the migration mode does not occur until about 400 K for helium diffusion in bcc Mo and about 450 K for all W–Mo alloys. Hence, most of the temperatures in the range of 300–1500 K are high enough to favor the T-O-T pathway and sample it more frequently than the T-T pathway for all alloy compositions. This conclusion is supported by observations from molecular dynamics (MD) calculations of helium in tungsten where a switch from the T-T pathway to the T-O-T pathway was reported with increasing temperature.[57]

TABLE IV. Calculated interstitial helium diffusivity in W–Mo heterogeneous and homogeneous binary alloys at 500 K and 1000 K.

	Diffusivity at 500 K (m^2/s)	Diffusivity at 1000 K (m^2/s)
Homogeneous alloy $W_{0.5}Mo_{0.5}$	9.9×10^{-10}	4.2×10^{-8}
W Grain interior and Mo outer region	2.3×10^{-8}	1.2×10^{-7}
Mo Grain interior and W outer grain region	3.2×10^{-12}	1.0×10^{-10}

Upon exposure of alloys to radiation, it is known that radiation-induced segregation of elements may occur.[58–60] This happens when radiation-induced point defects migrate to low

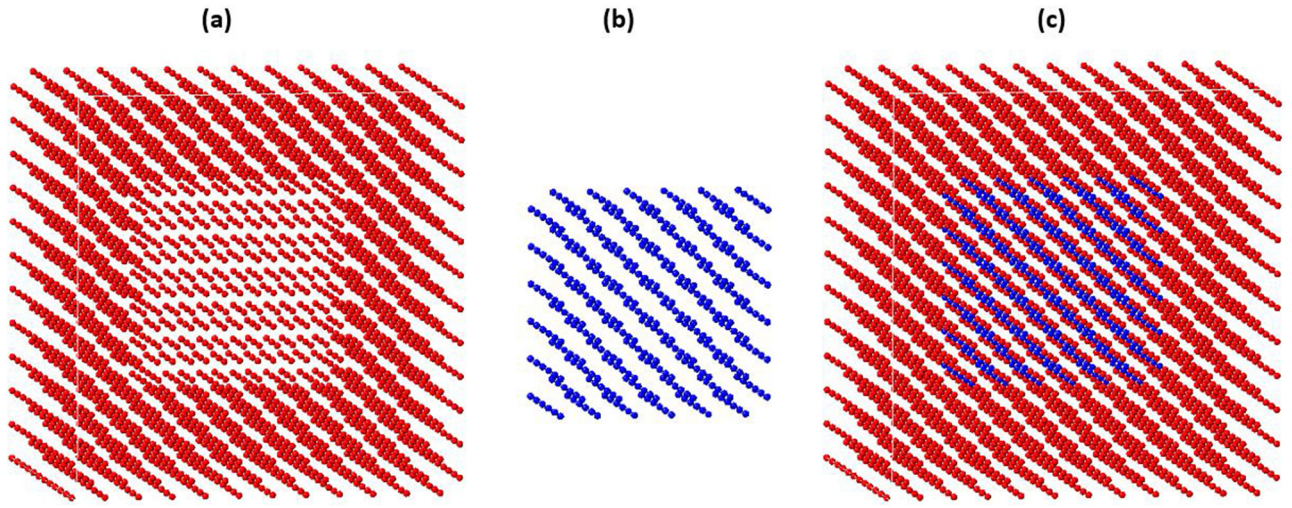

FIG. 9. An illustration of the structure being considered in the case of radiation-induced segregation of the binary alloy. These structures represent chemically segregated structures that were designed to mimic the effects of grain boundary segregation though no grain boundaries were explicitly considered here. (a) shows the exterior region of the computational supercell (element A); (b) shows the interior region of the computational supercell (element B); (c) shows the total structure.

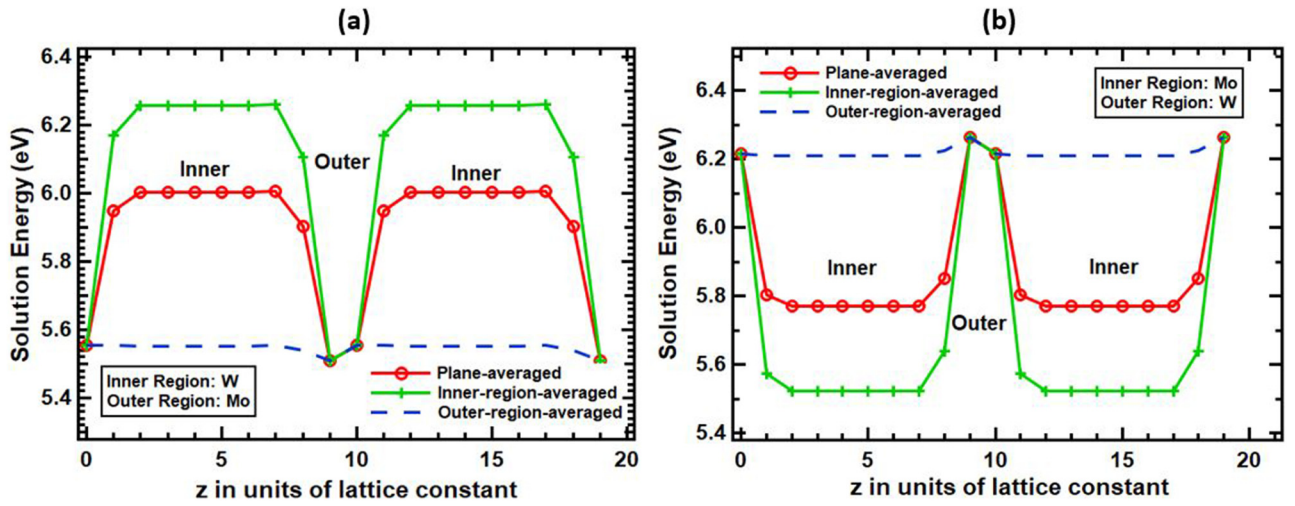

FIG. 10. A realization of the energy landscape for helium migration through the structure depicted in Fig. 9. (a) The case where W segregates to the inner region of the grain and Mo to the outer grain region. (b) The case where Mo segregates to the grain inner region and W to the grain outer region. The plane-averaged energies reported include the plane-averaged energy for every z (red line with circles), the plane-averaged energy taking into account only the path along the grain inner region (green line with + marks), and the plane-averaged energy for the path taken along the z direction traversing the grain outer region (blue dashed line).

energy sites such as grain boundaries thereby creating a defect flux, which may preferentially associate with an alloying element thereby leading to segregation.[60–62] This phenomenon has recently also been studied in tungsten alloys.[58,59,63] In order to further explore the kinetics of interstitial helium in the W–Mo alloy, we consider the case of radiation-induced segregation to simulate conditions that may arise in a fusion reactor. To mimic this effect, simulation structures in Fig. 9 were considered. Here, it is important to note that grain boundaries were not explicitly modeled in this work, but rather a compositional segregation pattern to mimic a situation that may arise upon radiation exposure. In one case, tungsten was localized to the interior of the computational cell and molybdenum to the outer region of the computational cell, and in the other case, the opposite situation was considered. kMC simulations were performed on these structures that consisted of $10 \times 10 \times 10$ supercells with an outer region thickness of one unit cell in each direction and an overall composition of roughly $W_{0.5}Mo_{0.5}$ as shown in Fig. 9.

Periodic boundary conditions and the blocking model were utilized in all simulations just as described previously, and the results were obtained by using 20 helium atoms and calculating the mean squared displacement at 500 K and 1000 K, which are included in Table IV. These results show that the helium migration for the case of a W grain interior and Mo outer grain region is much larger than the case of the homogeneous alloy whereas the migration for a situation with a Mo grain interior and a W outer grain region is slower. Due to the relatively low migration energies for interstitial helium reported (Table II) compared with the variations in the solution energy landscape observed in the alloy [a range of about 1 eV as shown in Fig. 4(a)], it is reasonable to assume (to first order) that the diffusion of the interstitial helium in the binary W–Mo alloy is dominated by the solution energy landscape. Hence, and to further analyze the observed results, an averaged energy landscape was plotted for both cases in Fig. 10.

For the case of a tungsten inner region and a molybdenum outer region [Fig. 10(a)], it is more favorable for the diffusing helium to move along the grain outer region (the green marked line) due to the low migration energy needed thereby completely avoiding the grain interior. The diffusivity values reported here are comparable to the values in bulk bcc Mo reported in Fig. 7. In the case when molybdenum segregates to the grain interior, and tungsten to the grain outer region, then the minimum energy pathway indicates that the helium atom becomes trapped in the molybdenum inner region and must overcome a large barrier of about 0.9 eV to escape from the grain inner region, only to get trapped in the next grain inner

TABLE V. The DFT calculated interstitial He–He interactions in bcc tungsten and molybdenum. The helium atoms were placed in first, second, and third nearest neighbor T-sites at the beginning of the simulation and the final He–He distance at the end of the calculation is reported.

He–He interactions	First nearest neighbor	Second nearest neighbor	Third nearest neighbor
W supercell (this work)	−0.83 eV (1.44 Å)	−1.04 eV (1.49 Å)	−1.10 eV (1.52 Å)
W (Becquart *et al.*)[26]	−0.74 eV (1.44 Å)	−0.94 eV (1.49 Å)	−1.01 eV (1.51 Å)
Mo supercell (this work)	−0.74 eV (1.49 Å)	−0.94 eV (1.54 Å)	−0.82 eV (1.58 Å)

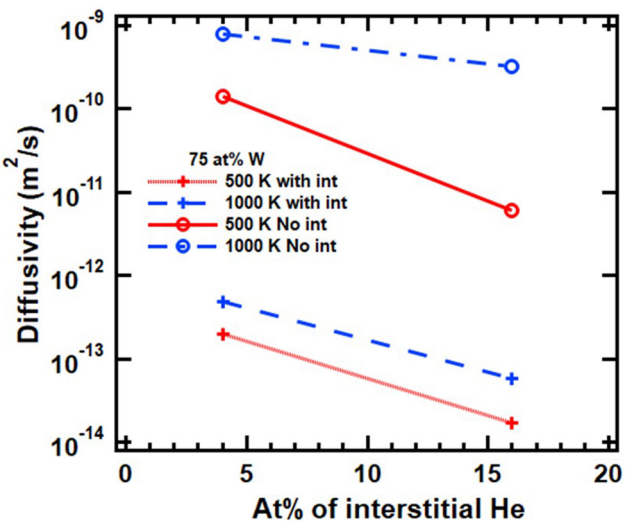

FIG. 11. Helium diffusivity in bcc W–Mo alloy (75 at. % W) taking into account the helium–helium interactions up to the second nearest neighbor shown for two different temperatures as a function of the amount of helium in the simulation [reported as at. % interstitial helium = (number of He/number of metal atoms)×100%].

region [green marked path in Fig. 10(b)], so the helium diffusion slows down compared with the homogeneous case.

In this work, helium–helium interactions had not been considered up to this point with the exception of the blocking model employed in all kMC simulations. In an effort to explore the kinetics of helium beyond the dilute level, DFT calculations were performed to obtain the helium–helium interaction energies in bulk bcc W and bulk bcc Mo for first nearest neighboring T-sites and second nearest neighboring T-sites. The energies were calculated by using Eq. (5),

$$E_{int} = E(\mathrm{A} + \mathrm{He}_2) + E(\mathrm{A}) - 2E(\mathrm{A} + \mathrm{He}) \quad \text{for} \quad \mathrm{A} = \mathrm{W\ or\ Mo}, \tag{5}$$

where $E(\mathrm{A}{-}\mathrm{He}_2)$ is the energy for the metal supercell with two helium atoms bound to T-sites, E(A) is the energy of the metallic supercell in the absence of helium, and $E(\mathrm{A}{-}\mathrm{He})$ is the energy of the metallic supercell with one interstitial helium atom bound to the tetrahedral site. All calculations were performed on $4 \times 4 \times 4$ supercells using the same settings described in the computational details. The results are included in Table V.

The reported results are consistent with those reported by Becquart and Domain[26] who used the PW91 density functional compared with the PBE density functional used in this work. It is clear that He–He interactions are relatively strong, attractive, and

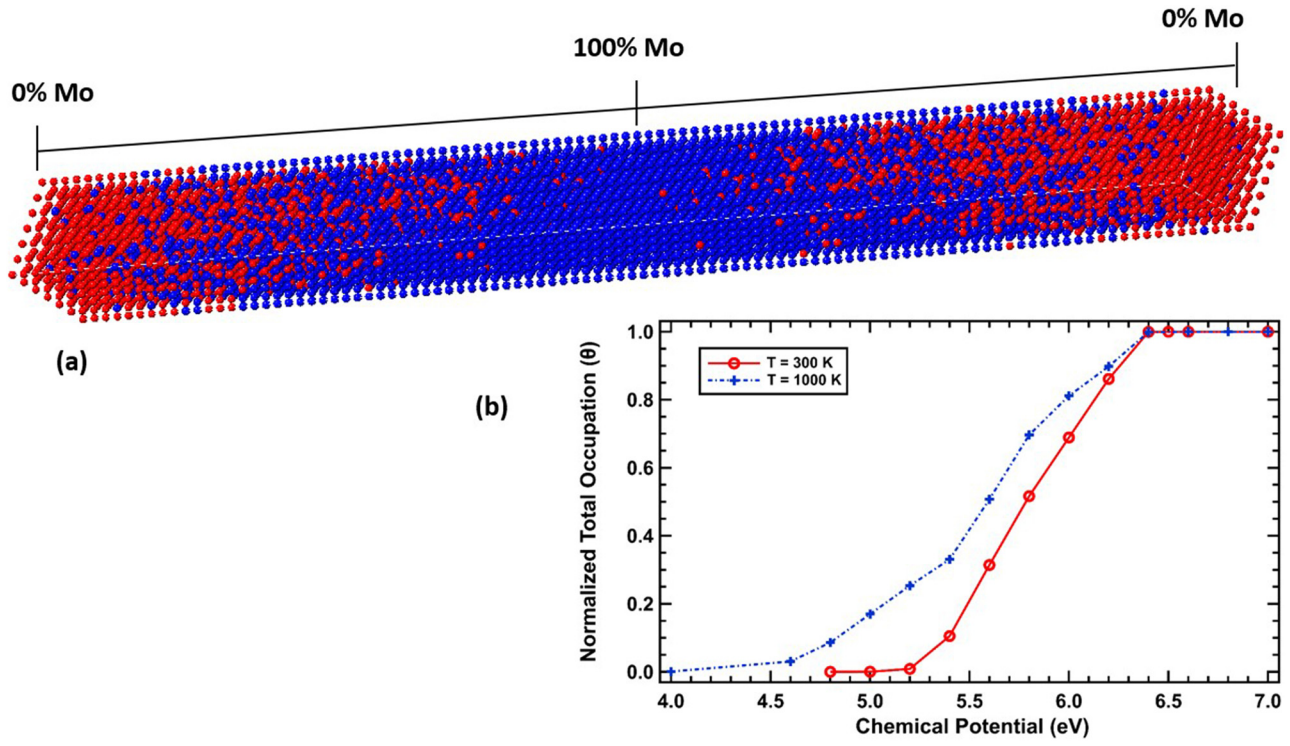

FIG. 12. (a) An illustration of the structure of the W–Mo supercell constructed for GCMC simulations. (b) The helium binding isotherms as functions of the chemical potential recorded for temperatures 300 K and 1000 K.

long range in both tungsten and Mo although they appear to be stronger in tungsten. Moreover, helium–helium interaction appears to be strongest for the third nearest neighbor for tungsten (of the calculations performed here), whereas the second nearest neighbor attractive force is strongest in the case of interstitial helium in bcc molybdenum. The results of Table V suggest that the strength of He–He interactions may be related to an optimum distance between the atoms. These strong attractive forces are expected to play a significant role in influencing the behavior of the helium in the metal beyond the dilute limit. In order to gain some insight into this, the interaction energies up to the second nearest neighbor were incorporated into the kMC model described earlier (with blocking) and a much higher fraction of helium atoms was considered. This was done by limiting the supercell size to $5 \times 5 \times 5$ unit cells and considering the case of 25 helium atoms and 100 helium atoms for two different temperatures. The results of this analysis were compared to the results of the same simulations performed without He–He interactions beyond the blocking model. The results are included in Fig. 11.

Upon inspection of Fig. 11, it is clear that considering these attractive interactions led to a significant reduction of the calculated diffusivity by several orders of magnitude. Therefore, and for helium concentrations beyond the dilute limit, it is important to consider these interactions as they can significantly impact the results. Furthermore, and beyond the dilute limit, it is important to consider cluster dynamics[64,65] where helium clusters begin to migrate with their own migration energies. While this topic is undoubtedly important, it is beyond the scope of this work, and we shall restrict ourselves to analyzing behavior in the dilute limit. Hence, it is important to emphasize that the results of the present work provide an important first step toward understanding the behavior of helium in W–Mo alloys and further yield important input parameters needed for higher level models (such as cluster dynamics models or others).[64,65]

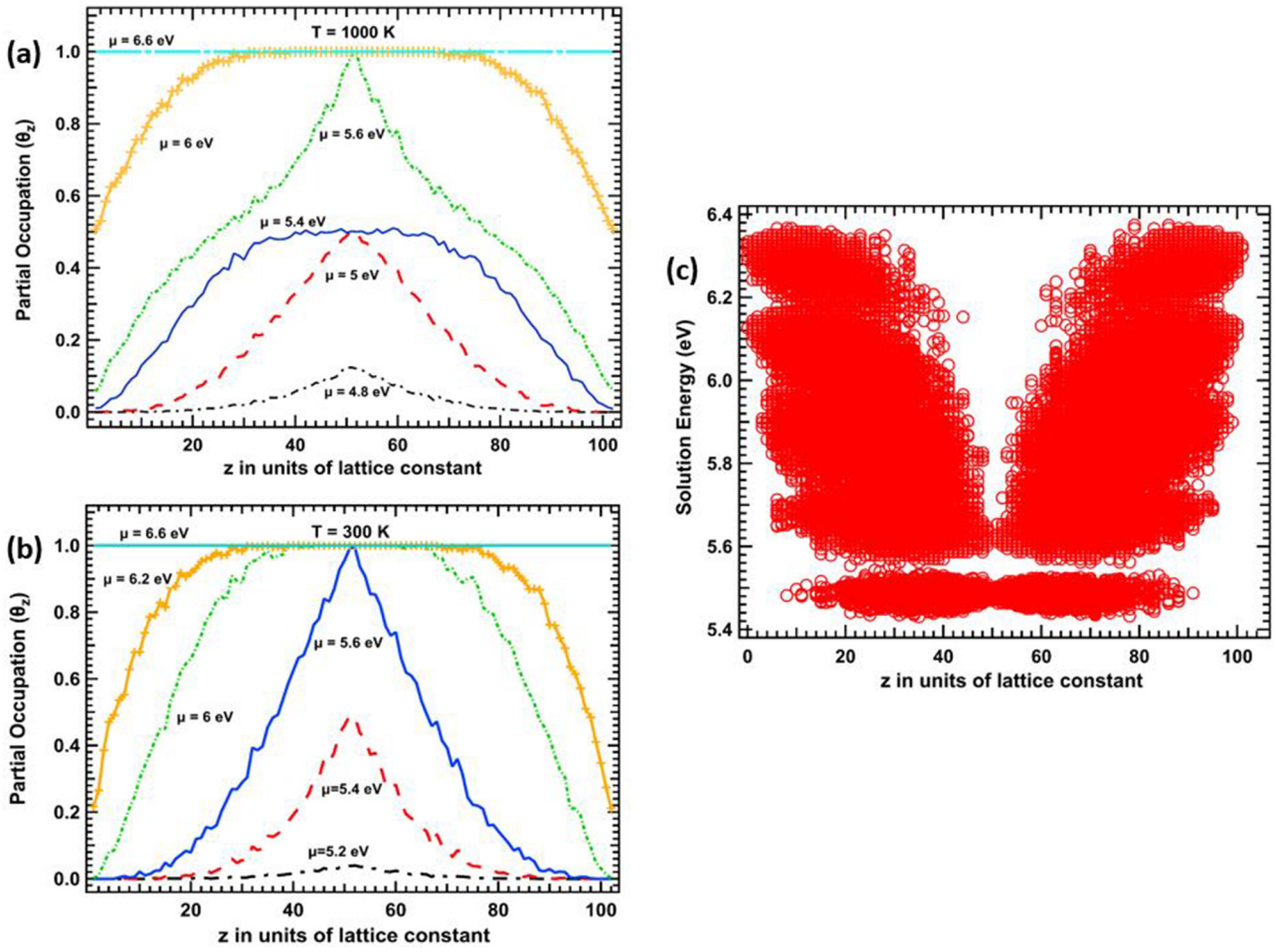

FIG. 13. (a) Helium plane-averaged occupation profile as a function of the z coordinate shown for several values of the chemical potential at T = 300 K. (b) Helium plane-averaged occupation profile as a function of the z coordinate shown for several values of the chemical potential at T = 1000 K. (c) The helium solution energy landscape in the supercell as a function of the z coordinate.

Next, the neural network model for the helium solution energy in W–Mo binary alloys was used in conjunction with Grand Canonical Monte Carlo (GCMC) simulations to examine the thermodynamic behavior of helium in the alloy. A supercell of size $8 \times 8 \times 102$ unit cells was constructed with a gradually varied composition from 100 at. % Mo to 100 at. % W and back to 100 at. % Mo along the z direction in order to apply periodic boundary conditions (PBCs) in all directions. At each z level, the Mo concentration was specified (varied by 2 at. %) and a number of atoms corresponding to that concentration was randomly chosen and assigned as Mo. GCMC simulations[66] were performed on this supercell at two different temperatures, 300 K and 1000 K. An illustration of the supercell is included in Fig. 12(a), and the binding isotherms recorded for the two temperatures are shown in Fig. 12(b). The total occupation was defined as the number of helium atoms normalized by the number of available T-sites in the system. From Fig. 12(b), it is clear that helium uptake begins at a lower helium chemical potential (corresponding to a lower helium partial pressure) for the higher temperature case.

To gain better insight into the thermodynamic behavior of helium in binary W–Mo alloys, snapshots of the helium occupation profiles were analyzed, averaged over 5000 sweeps and plotted for several chemical potentials as a function of temperature, and these results are included in Figs. 13(a) and 13(b). The energy landscape is illustrated in Fig. 13(c).

Figures 13(a) and 13(b) indicate that the interstitial helium binds all the Mo-rich regions in the middle of the supercell and then gradually occupies other sites, and the sites at the two ends of the simulation cell (with 100 at. % W) are the last to be filled so that at large enough helium chemical potential, all available binding sites are occupied. This behavior can be explained by observing the helium solution energy landscape included in Fig. 13(c). This figure shows that all the sites in the middle of the supercell have their energies clustered about 5.5 eV and 5.6 eV. This is why we see that for both temperatures [Figs. 13(a) and 13(b)], the occupation profile with chemical potential 5.6 eV has a partial occupation of unity for z located in the middle of the supercell and that the occupation profile in this middle section suddenly jumps from partial occupation of 0.5 to partial occupation of 1.

CONCLUSIONS

Tungsten alloys are actively being sought as potential materials to be used for plasma-facing components in fusion reactors due to their superior properties. One of the important challenges in developing plasma-facing materials for fusion reactors is their ability to withstand the interaction with energetic helium ions, which can escape from the plasma and undermine material integrity. In the present study, an artificial neural network was trained with a database consisting of 120 DFT calculations to predict helium solution energies in the binary W–Mo alloys as a function of the local environment. The neural network was able to reproduce the DFT values with a RMSE of 0.035 eV. The prediction power of the neural network was tested by leaving out 15% of the data points and calculating a cross validation score. This yielded a CV score of 0.04 eV, and different values of the parameters were found to be centered about the optimum value indicating a stable fit. The trained neural network was then utilized in a kinetically resolved activation barrier (kRA) model with blocking, and the diffusivity of interstitial helium was examined over the entire range of homogeneous W–Mo alloys going from 0 at. % W to 100 at. % W. It was observed that alloy composition may significantly affect interstitial helium diffusion with the slowest diffusion occurring in homogeneous alloys with compositions in the range of 75–90 at. % W. Arrhenius fits of the recorded diffusivities showed that helium diffusion in bulk bcc tungsten and molybdenum was dominated by the T-O-T pathway for the chosen temperatures (300–1500 K). A sequence of kMC simulations tracking the trajectory of an interstitial helium atom in W–Mo alloys indeed confirmed that the T-T pathway dominates diffusion for low temperatures. The switch to a T-O-T-dominated pathway was shown to occur around 250 K for interstitial He diffusion in bulk bcc tungsten and by 450 K for all W–Mo alloy compositions. Diffusion in heterogeneous structures was also considered to account for situations of radiation-induced segregation, and it was found that helium diffusion was fast for cases where tungsten segregated to the grain inner region and molybdenum to the grain outer region and was slow for the reverse situation. These observations were explained on the basis of the energy landscape. In the former case, it was energetically favorable for the helium to travel via a network of grain outer regions thereby completely avoiding the grain interior, whereas in the latter case, the helium became trapped in the grain inner region and needed to overcome a large barrier to escape the grain interior. Interstitial helium–helium interactions were calculated to be strong, attractive, and long range in both W and Mo consistent with previous work. In addition, these interactions were shown to significantly impact the diffusion behavior of helium. Finally, an investigation of the binding isotherm showed that areas of the alloy rich in Mo are thermodynamically most favorable for helium binding and may be the initiation point for helium bubbles in the material. The results of this study may provide useful input for higher level cluster dynamics models[64,65] and inform the design of next generation materials for plasma-facing components.

ACKNOWLEDGMENTS

This work was partially supported by allocations of computational resources from the Ohio Supercomputing Center (OSC) and from the DOD HPC systems. In addition, the author would like to acknowledge support from the AFIT Faculty Research Council.

APPENDIX: DETAILS OF THE GENETIC ALGORITHM USED TO ASSIST IN THE SELECTION OF ADDITIONAL STRUCTURES FOR THE DFT DATABASE

Here we will give a description of the genetic algorithm mentioned in the computational section which was used to aid in generating input for DFT calculations. The genomes in our problem represent $4 \times 4 \times 4$ supercells of W–Mo binary alloys. In this implementation, the overall composition of the alloy was fixed at the beginning of the simulation W_xMo_{1-x} (with the number of tungsten atoms specified at the beginning of the simulation and fixed throughout). Binary values were used to specify the genome of an individual with (+1) for tungsten and (−1) for molybdenum. The population size, that is, the number of genomes used, determines the amount of genetic diversity. In this implementation, we used

$N_{pop} = 12$. The survival rate for the candidate genomes was set at 4/12 and that meant that at the end of each generation the individuals were ranked and only four members with the best fitness were retained for the next generation. The way fitness was determined was by computing the helium solution energies for all the T-sites in the supercell and selecting the minimum value and the four individuals with the lowest solution energies were retained for the next generation. To create a child, two parents were randomly selected from the existing generation and then one by one the individual genes of the child genome were selected from parent 1 or 2 with probabilities proportional to the fitness of these two parents with the genes of the fitter parent (the one associated with the lower solution energy) having a higher probability of being selected to ensure passing on better genetic information. Furthermore, and after each mating step, mutations could occur and each gene was allowed to change from 1 to −1 or vice versa with a low mutation probability (0.15 was used in this work). Of course, this process may ultimately lead to a child whose composition does not match the one specified at the beginning of the simulation. Therefore, and after the creation of each child, its genome was checked, and if it differed from the required composition, then an appropriate number of (+1) genes would be randomly selected and flipped to (−1) or vice versa so that the required overall composition of the binary alloy is achieved. This process was allowed to occur for 1000 generations to obtain the supercell and the T-site within this supercell associated with the most favorable helium solution energy. This process was repeated three times for each composition, and the results were used in DFT calculations and added to the DFT database used to train the artificial neural network.

REFERENCES

[1]M. Zucchetti, "The zero-waste option for nuclear fusion reactors: Advanced fuel cycles and clearance of radioactive materials," Ann. Nucl. Energy **32**, 1584–1593 (2005).

[2]T. Muroga, M. Gasparotto, and S. J. Zinkle, "Overview of materials research for fusion reactors," Fusion Eng. Des. **61–62**, 13–25 (2002).

[3]H. Bolt, V. Barabash, W. Krauss, J. Linke, R. Neu, S. Suzuki, and N. Yoshida, "Materials for the plasma-facing components of fusion reactors," J. Nucl. Mater. **329–333**, 66–73 (2004).

[4]G. Pintsuk, "Tungsten as a plasma-facing material," in *Comprehensive Nuclear Materials* (Elsevier Ltd., 2012), pp. 551–581.

[5]K. Tokunaga, M. J. Baldwin, R. P. Doerner, N. Noda, Y. Kubota, N. Yoshida, T. Sogabe, T. Kato, and B. Schedler, "Blister formation and deuterium retention on tungsten exposed to low energy and high flux deuterium plasma," J. Nucl. Mater. **337–339**, 887–891 (2005).

[6]P. E. Lhuillier, T. Belhabib, P. Desgardin, B. Courtois, T. Sauvage, M. F. Barthe, A. L. Thomann, P. Brault, and Y. Tessier, "Helium retention and early stages of helium-vacancy complexes formation in low energy helium-implanted tungsten," J. Nucl. Mater. **433**, 305–313 (2013).

[7]J. Marian, C. S. Becquart, C. Domain, S. L. Dudarev, M. R. Gilbert, R. J. Kurtz, D. R. Mason, K. Nordlund, A. E. Sand, L. L. Snead, T. Suzudo, and B. D. Wirth, "Recent advances in modeling and simulation of the exposure and response of tungsten to fusion energy conditions," Nucl. Fusion **57**, 092008 (2017).

[8]K. D. Hammond, "Helium, hydrogen, and fuzz in plasma-facing materials," Mater. Res. Express. **4**, 104002 (2017).

[9]R. Ohser-Wiedemann, U. Martin, A. Müller, and G. Schreiber, "Spark plasma sintering of Mo-W powders prepared by mechanical alloying," J. Alloys Compd. **560**, 27–32 (2013).

[10]D. Jiang, Q. Zhou, L. Xue, T. Wang, and J. Hu, "First-principles study the phase stability and mechanical properties of binary W-Mo alloys," Fusion Eng. Des. **130**, 56–61 (2018).

[11]A. K. Srivastav, N. Chawake, D. Yadav, N. S. Karthiselva, and B. S. Murty, "Localized pore evolution assisted densification during spark plasma sintering of nanocrystalline W-5 wt. %Mo alloy," Scr. Mater. **159**, 41–45 (2019).

[12]P. K. Sahoo, S. K. Srivastava, S. S. K. Kamal, and L. Durai, "Consolidation behavior of W–20–40 wt. % Mo nanoalloys synthesized by thermal decomposition method," Int. J. Refract. Met. Hard Mater. **51**, 124–129 (2015).

[13]A. Xu, D. E. J. Armstrong, C. Beck, M. P. Moody, G. D. W. Smith, P. A. J. Bagot, and S. G. Roberts, "Ion-irradiation induced clustering in W-Re-Ta, W-Re and W-Ta alloys: An atom probe tomography and nanoindentation study," Acta Mater. **124**, 71–78 (2017).

[14]S. Watanabe, S. Nogami, J. Reiser, M. Rieth, S. Sickinger, S. Baumgärtner, T. Miyazawa, and A. Hasegawa, "Tensile and impact properties of tungsten-rhenium alloy for plasma-facing components in fusion reactor," Fusion Eng. Des. **148**, 111323 (2019).

[15]D. Jiang, Q. Zhou, W. Liu, T. Wang, and J. Hu, "First-principles study the structures and mechanical properties of binary W-V alloys," Physica B **552**, 165–169 (2019).

[16]R. Zhang, H. Zhou, J. Yu, W. Han, M. Liu, C. Chen, and K. Zhu, "Effect of vanadium alloying on irradiation performance of tungsten under 60 keV helium irradiation," J. Nucl. Mater. **512**, 65–71 (2018).

[17]L. Buzi, M. Yeh, Y. W. Yeh, O. K. Donaldson, M. I. Patino, J. R. Trelewicz, N. Yao, R. Doerner, and B. E. Koel, "Deuterium and helium ion irradiation of nanograined tungsten and tungsten–titanium alloys," Nucl. Mater. Energy **21**, 100713 (2019).

[18]R. Mateus, M. Dias, J. Lopes, J. Rocha, N. Catarino, P. Duarte, R. B. Gomes, C. Silva, H. Fernandes, V. Livramento, P. A. Carvalho, E. Alves, K. Hanada, and J. B. Correia, "Blistering of W-Ta composites at different irradiation energies," J. Nucl. Mater. **438**, S1032–S1035 (2013).

[19]J. Cao, J. Liu, C. He, S. Li, Z. Hao, and X. Xue, "Enhanced ductility of W–Mo–Cu alloy through the formation of nanometer-to-micrometer-thick dual-phase transition phase layer," Mater. Des. **164**, 107536 (2019).

[20]O. El-Atwani, N. Li, M. Li, A. Devaraj, J. K. S. Baldwin, M. M. Schneider, D. Sobieraj, J. S. Wróbel, D. Nguyen-Manh, S. A. Maloy, and E. Martinez, "Outstanding radiation resistance of tungsten-based high-entropy alloys," Sci. Adv. **5**, eaav2002 (2019).

[21]A. Hasegawa, M. Fukuda, K. Yabuuchi, and S. Nogami, "Neutron irradiation effects on the microstructural development of tungsten and tungsten alloys," J. Nucl. Mater. **471**, 175–183 (2016).

[22]F. Ferroni, K. D. Hammond, and B. D. Wirth, "Sputtering yields of pure and helium-implanted tungsten under fusion-relevant conditions calculated using molecular dynamics," J. Nucl. Mater. **458**, 419–424 (2015).

[23]S. Blondel, D. E. Bernholdt, K. D. Hammond, and B. D. Wirth, "Continuum-scale modeling of helium bubble bursting under plasma-exposed tungsten surfaces," Nucl. Fusion **58**, 126034 (2018).

[24]D. Perez, L. Sandoval, S. Blondel, B. D. Wirth, B. P. Uberuaga, and A. F. Voter, "The mobility of small vacancy/helium complexes in tungsten and its impact on retention in fusion-relevant conditions," Sci. Rep. **7**, 2522 (2017).

[25]S. Das, D. E. J. Armstrong, Y. Zayachuk, W. Liu, R. Xu, and F. Hofmann, "The effect of helium implantation on the deformation behaviour of tungsten: X-ray micro-diffraction and nanoindentation," Scr. Mater. **146**, 335–339 (2018).

[26]C. S. Becquart and C. Domain, "Migration energy of He in W revisited by *ab initio* calculations," Phys. Rev. Lett. **97**, 196402 (2006).

[27]R. W. Harrison, G. Greaves, J. A. Hinks, and S. E. Donnelly, "Engineering self-organising helium bubble lattices in tungsten," Sci. Rep. **7**, 7724 (2017).

[28]L. Sandoval, D. Perez, B. P. Uberuaga, and A. F. Voter, "Formation of helium-bubble networks in tungsten," Acta Mater. **159**, 46–50 (2018).

[29]H. Chen, X. Zhan, X. Liu, Y. Hai, J. Xu, T. Zhu, and W. Yin, "The behavior of helium atoms in He+ ion implanted W/Ni bilayer nanocomposite," Appl. Surf. Sci. **486**, 274–280 (2019).

[30]X. Wu, X.-S. Kong, Y.-W. You, C. S. Liu, Q. F. Fang, J.-L. Chen, G.-N. Luo, and Z. Wang, "Effects of alloying and transmutation impurities on stability and mobility of helium in tungsten under a fusion environment," Nucl. Fusion **53**, 073049 (2013).
[31]X. Wu, X. S. Kong, Y. W. You, C. S. Liu, Q. F. Fang, J. L. Chen, G. N. Luo, and Z. Wang, "First principles study of helium trapping by solute elements in tungsten," J. Nucl. Mater. **455**, 151–156 (2014).
[32]P. E. Blöchl, "Projector augmented-wave method," Phys. Rev. B **50**, 17953–17979 (1994).
[33]G. Kresse and D. Joubert, "From ultrasoft pseudopotentials to the projector augmented-wave method," Phys. Rev. B **59**, 1758–1775 (1999).
[34]G. Kresse and J. Furthmüller, "Efficiency of ab-initio total energy calculations for metals and semiconductors using a plane-wave basis set," Comput. Mater. Sci. **6**, 15–50 (1996).
[35]G. Kresse and J. Furthmüller, "Efficient iterative schemes for ab initio total-energy calculations using a plane-wave basis set," Phys. Rev. B **54**, 11169–11186 (1996).
[36]M. C. Payne, M. P. Teter, D. C. Allan, T. A. Arias, and J. D. Joannopoulos, "Iterative minimization techniques for ab initio total-energy calculations: Molecular dynamics and conjugate gradients," Rev. Mod. Phys. **64**, 1045–1097 (1992).
[37]J. P. Perdew, K. Burke, and M. Ernzerhof, "Generalized gradient approximation made simple," Phys. Rev. Lett. **77**, 3865–3868 (1996).
[38]M. Methfessel and A. T. Paxton, "High-precision sampling for Brillouin-zone integration in metals," Phys. Rev. B **40**, 3616–3621 (1989).
[39]H. J. Monkhorst and J. D. Pack, "Special points for Brillouin-zone integrations," Phys. Rev. B **13**, 5188–5192 (1976).
[40]G. Henkelman, B. P. Uberuaga, and H. Jónsson, "A climbing image nudged elastic band method for finding saddle points and minimum energy paths," J. Chem. Phys. **113**, 9901–9904 (2000).
[41]G. Henkelman and H. Jónsson, "Improved tangent estimate in the nudged elastic band method for finding minimum energy paths and saddle points," J. Chem. Phys. **113**, 9978–9985 (2000).
[42]H. Jónsson, G. Mills, and K. W. Jacobsen, *Nudged Elastic Band Method for Finding Minimum Energy Paths of Transitions* (World Scientific Pub. Co. Pte Ltd., 1998), pp. 385–404.
[43]A. J. Samin, D. A. Andersson, E. F. Holby, and B. P. Uberuaga, "First-principles localized cluster expansion study of the kinetics of hydrogen diffusion in homogeneous and heterogeneous Fe-Cr alloys," Phys. Rev. B **99**, 14110 (2019).
[44]R. Rojas, *Neural Networks: A Systematic Introduction*, 1st ed. (Springer, 1996).
[45]P. Kim, "Machine learning," in *MATLAB Deep Learning* (Apress, Berkeley, CA, 2017), pp. 1–18.
[46]S. C. Lee, J. H. Choi, and J. G. Lee, "Energetics of He and H atoms with vacancies in tungsten: First-principles approach," J. Nucl. Mater. **383**, 244–246 (2009).
[47]X. T. Zu, L. Yang, F. Gao, S. M. Peng, H. L. Heinisch, X. G. Long, and R. J. Kurtz, "Properties of helium defects in bcc and fcc metals investigated with density functional theory," Phys. Rev. B **80**, 054104 (2009).
[48]W. M. Haynes, D. R. Lide, and T. J. Bruno, See http://public.eblib.com/choice/publicfullrecord.aspx?p=4711508 for "CRC handbook of chemistry and physics: A ready-reference book of chemical and physical data" (2017).
[49]J. P. Perdew, J. A. Chevary, S. H. Vosko, K. A. Jackson, M. R. Pederson, D. J. Singh, and C. Fiolhais, "Atoms, molecules, solids, and surfaces: Applications of the generalized gradient approximation for exchange and correlation," Phys. Rev. B **46**, 6671–6687 (1992).
[50]Q. Zhao, Z. Zhang, Y. Li, and X. Ouyang, "First-principles study on various point defects formed by hydrogen and helium atoms in tungsten," Sci. Technol. Nucl. Install. **2017**, 1–9.
[51]O. Runevall and N. Sandberg, "Helium cluster dissolution in molybdenum," J. Phys. Condens. Matter. **21**, 335401 (2009).
[52]Y. W. You, X. S. Kong, X. B. Wu, Q. F. Fang, J. L. Chen, G. N. Luo, and C. S. Liu, "Effect of vacancy on the dissolution and diffusion properties of hydrogen and helium in molybdenum," J. Nucl. Mater. **433**, 167–173 (2013).
[53]N. Zhang, Y. Zhang, Y. Yang, P. Zhang, Z. Hu, and C. Ge, "Trapping of helium atom by vacancy in tungsten: A density functional theory study," Eur. Phys. J. B **90**, 105 (2017).
[54]G. H. Vineyard, "Frequency factors and isotope effects in solid state rate processes," J. Phys. Chem. Solids. **3**, 121–127 (1957).
[55]A. Van der Ven, G. Ceder, M. Asta, and P. D. Tepesch, "First-principles theory of ionic diffusion with nondilute carriers," Phys. Rev. B **64**, 184307 (2001).
[56]B. Puchala and D. Morgan, "Atomistic modeling of as diffusion in ZnO," Phys. Rev. B **85**, 064106 (2012).
[57]X. Shu, P. Tao, X. Li, and Y. Yu, "Helium diffusion in tungsten: A molecular dynamics study," Nucl. Instrum. Methods Phys. Res. Sect. B **303**, 84–86 (2013).
[58]J. S. Wróbel, D. Nguyen-Manh, K. J. Kurzydłowski, and S. L. Dudarev, "A first-principles model for anomalous segregation in dilute ternary tungsten-rhenium-vacancy alloys," J. Phys. Condens. Matter **29**, 145403 (2017).
[59]L. Gharaee, J. Marian, and P. Erhart, "The role of interstitial binding in radiation induced segregation in W-Re alloys," J. Appl. Phys. **120**, 025901 (2016).
[60]G. S. Was, J. P. Wharry, B. Frisbie, B. D. Wirth, D. Morgan, J. D. Tucker, and T. R. Allen, "Assessment of radiation-induced segregation mechanisms in austenitic and ferritic-martensitic alloys," J. Nucl. Mater. **411**, 41–50 (2011).
[61]C. M. Barr, P. J. Felfer, J. I. Cole, and M. L. Taheri, "Observation of oscillatory radiation induced segregation profiles at grain boundaries in neutron irradiated 316 stainless steel using atom probe tomography," J. Nucl. Mater. **504**, 181–190 (2018).
[62]O. Senninger, F. Soisson, E. Martínez, M. Nastar, C.-C. Fu, and Y. Bréchet, "Modeling radiation induced segregation in iron-chromium alloys," Acta Mater. **103**, 1–11 (2016).
[63]A. Xu, C. Beck, D. E. J. Armstrong, K. Rajan, G. D. W. Smith, P. A. J. Bagot, and S. G. Roberts, "Ion-irradiation-induced clustering in W-Re and W-Re-Os alloys: A comparative study using atom probe tomography and nanoindentation measurements," Acta Mater. **87**, 121–127 (2015).
[64]S. I. Krasheninnikov, T. Faney, and B. D. Wirth, "On helium cluster dynamics in tungsten plasma facing components of fusion devices," Nucl. Fusion **54**, 073019 (2014).
[65]Y. G. Li, W. H. Zhou, L. F. Huang, Z. Zeng, and X. Ju, "Cluster dynamics modeling of accumulation and diffusion of helium in neutron irradiated tungsten," J. Nucl. Mater. **431**, 26–32 (2012).
[66]S. Alavi, in *Statistical Mechanics Theory and Molecular Simulation*, edited by M. E. Tuckerman (Oxford University Press, 2011).